

Research Paper

Decomposed Infrared Luminosity Functions of High-Redshift Galaxies and AGN using CIGALE

Daniel J. Lyon¹, Oliver Pye¹, Michael J. Cowley¹, and Andrew M. Hopkins²

¹School of Chemistry and Physics, Queensland University of Technology, Brisbane, QLD, Australia

²Australian Astronomical Optics, Macquarie University, North Ryde, NSW, Australia

Abstract

Lorem ipsum dolor sit amet, consectetuer adipiscing elit. Ut purus elit, vestibulum ut, placerat ac, adipiscing vitae, felis. Curabitur dictum gravida mauris. Nam arcu libero, nonummy eget, consectetuer id, vulputate a, magna. Donec vehicula augue eu neque. Pellentesque habitant morbi tristique senectus et netus et malesuada fames ac turpis egestas. Mauris ut leo. Cras viverra metus rhoncus sem. Nulla et lectus vestibulum urna fringilla ultrices. Phasellus eu tellus sit amet tortor gravida placerat. Integer sapien est, iaculis in, pretium quis, viverra ac, nunc. Praesent eget sem vel leo ultrices bibendum. Aenean faucibus. Morbi dolor nulla, malesuada eu, pulvinar at, mollis ac, nulla. Curabitur auctor semper nulla. Donec varius orci eget risus. Duis nibh mi, congue eu, accumsan eleifend, sagittis quis, diam. Duis eget orci sit amet orci dignissim rutrum.

Keywords: galaxies: luminosity function, mass function; cosmology: observations; infrared: galaxies; galaxies: evolution

(Received xx xx xxxx; revised xx xx xxxx; accepted xx xx xxxx)

1. Introduction

In section 2 we ... In section 3 we ... In section 4 we ... In section 5 we ... In section 6 we ...

This paper is the first in a 2-part series, with the second looking at the ZFOURGE AGN LF and our approach to using CIGALE to decompose the IR SED and purely recover the AGN component.

We adopt a cosmology of $H_0 = 70 \text{ km s}^{-1} \text{ Mpc}^{-1}$, $\Omega_m = 0.7$, and $\Omega_\Lambda = 0.3$.

Research by Wu et al. (2011) has shown that the UV and optical wavelengths closely follow a Schechter function. In contrast, the IR wavelengths have a shallower exponential which is inconsistent with a Schechter function. Fu et al. (2010) proposed that this difference is due to the AGN contribution to the IR Galaxy LF. Even though this research primarily focuses on IR AGN LFs, it is essential to compare the IR Galaxy LF differences which this paper focuses on. In the next paper, we dive into IR AGN LFs.

Galaxy luminosity distribution and the environment have often been used to provide strong constraints of theories of galaxy evolution Biviano et al. (2011)

powerful constraints on how galaxies evolve in relation to their environment are expected to be obtained from the analysis of the galaxy IR LFs. Biviano et al. (2011)

IR data can give information only for dusty massive galaxies and are limited especially at high redshifts Katsianis et al. (2017)

alpha, the faint end slope of the galaxy LF, does not evolve significantly with redshift. Wylezalek et al. (2014)

Confirm that evolution on both luminosity and density is required to explain the difference in the LFs at different redshifts. Wu et al. (2011)

Extensively studied at low redshift. Wu et al. (2011)

SF may also heat the dust in galaxies and lead to excess emission in the longer wavelengths O'Connor et al. (2016)

The SF fraction is also found to be a function of luminosity/redshift, decreasing as luminosity or redshift increases, while the trend is more obvious in the MIR, suggesting that the MIR wavelength is more sensitive to the presence of AGNs Wu et al. (2011)

Star forming galaxies reemit a significant portion of the ultraviolet and optical radiation absorbed by dust in the infrared regime. Symeonidis & Page (2021); Fu et al. (2010)

The obscured or absorbed optical, UV and X-ray radiation will be re-emitted in the IR. Han et al. (2012); Brown et al. (2019)

The IR-bright, dust obscured galaxy population is crucial to understanding galaxy formation and evolution. Gruppioni et al. (2011)

IR bright galaxies emit the bulk of their energy as dust-reprocessed light generated by dusty SF or accretion onto the supermassive black holes referred to hereafter as active galactic nuclei. Wu et al. (2011)

Absorption by dust reprocesses the shorter wavelength radiation from the accretion disk into mid/far-IR continuum radiation. Assef et al. (2011)

The evolution of star formation activity in galaxies over cosmic history, and the physical process which may drive and limit such activity, have been the subject of intense observational and theoretical study in recent years. Grazian et al. (2015)

Author for correspondence: Daniel Lyon, Email: daniellyon31@gmail.com

Cite this article: Author1 C and Author2 C, an open-source python tool for simulations of source recovery and completeness in galaxy surveys. *Publications of the Astronomical Society of Australia* **00**, 1–12. <https://doi.org/10.1017/pasa.xxxx.xx>

2. The ZFOURGE Survey

2.1. Overview

The data for analysis is readily accessible through the ZFOURGE database at VizieR^a (Straatman et al. 2016). This dataset encompasses all three 11×11 arcminute fields within the ZFOURGE survey: the Chandra Deep Field South (CDFS), located at coordinates RA: 10h 00m 31s and DEC: $+02^\circ 17' 03''$ (Giacconi et al. 2002); the Cosmic Evolution Survey (COSMOS), located at RA: 03h 32m 27s and DEC: $-27^\circ 45' 52''$ (Scoville et al. 2007); and the CANDELS Ultra Deep Survey (UDS), located at RA: 02h 17m 15s and DEC: $-05^\circ 11' 53''$ (Lawrence et al. 2007). To ensure a comprehensive selection of candidate galaxies and minimise errors, the sole criterion applied is the Use=1 category, ensuring the inclusion of well-defined galaxies based on redshift, distance, magnitude, and other characteristics. The ZFOURGE dataset extends up to redshift $z \simeq 6$, providing a broad view across different epochs, particularly within the critical cosmic periods around $1 < z < 3$ (Gruppioni et al. 2011; Wylezalek et al. 2014), where luminous density peaks before diminishing (Assef et al. 2011).

Our analysis is based on galaxies from the 2017 release of the ZFOURGE survey (Straatman et al. 2016). This survey comprises approximately 70,000 galaxies at redshifts greater than 0.1, observed using the near-infrared FourStar imager (Persson et al. 2013) mounted on the 6.5-m Magellan Baade Telescope at the Las Campanas Observatory in Chile. ZFOURGE employs deep near-infrared imaging in multiple medium-band filters (J1, J2, J3, H1, Hs) and a broad-band Ks filter. The imaging spans 1.0 to $1.8 \mu\text{m}$ and achieves 5σ point-source limiting depths of 26 AB mag in the J medium-bands and 25 AB mag in the H and Ks bands (Spitler et al. 2012). These filters yield well-constrained photometric redshifts, particularly effective for sources within the redshift range of 1 to 4 (Spitler et al. 2012). ZFOURGE data is supplemented by public data from HST/WFC3 F160W and F125W imaging from the CANDELS survey, as well as data from Spitzer/Infrared Array Camera (IRAC) and Herschel/Photodetector Array Camera and Spectrometer (PACS). For a detailed description of the data and methodology, refer to Straatman et al. (2016).

2.2. Sample Selection

The three combined field, CDFS, COSMOS, and UDS have a combined total of 73,790 unique galaxies, but we employ some data reduction techniques to improve the quality of final dataset. First, we limit our sample to galaxies well defined by many factors such as sign-to-noise ratio, removing stars, bad detections, good redshifts, and more. This is given by keeping all sources with the column Use=1 in the dataset and immediately reduces the sample to 37,647 galaxies. Additionally, we keep all sources with a bolometric IR ($8\text{-}1000\mu\text{m}$) luminosity $L_{bol} > 0$. This is a simple data mask that only keeps galaxies whose bolometric IR luminosity has been successfully calculated and has further reduced our dataset to 22,997 galaxies. Finally, we utilise the ZFOURGE AGN catalogues provided by Cowley et al. (2016) to remove AGN from our sample. The AGN catalogues are similar to the Use data column with three new columns of irAGN, radAGN, and xAGN where a 1 in any column denotes a positive AGN. These three columns are ORed together and 552 galaxies across the three fields are removed, leaving a sample of 22,472 galaxies.

^aZFOURGE Data: <http://vizier.cds.unistra.fr/viz-bin/VizieR?-source=J/ApJ/830/51&to=2>

ZFOURGE can stretch up to redshift $z \simeq 6$, (with the highest redshift in the sample detected all the way out to $z = 7.9691$; only 28 galaxies greater than $z = 6$ exist in our reduced ZFOURGE dataset) allowing us to study a wide range of epochs. Our final sample includes 22,444 galaxies. This data range enables us to observe the evolution of galaxies during some of the most critical cosmic periods, specifically around $1 < z < 3$ (Gruppioni et al. 2011; Wylezalek et al. 2014). In the following section we detail the process of calculating the bolometric IR luminosity.

We use the UVJ colour-colour diagram to differentiate between quiescent and star-forming galaxies by selecting a quiescent galaxy mask with equation 1 (Cowley et al. 2016). better reference? Where U, V, & J are the rest-frame Johnson U, V and 2MASS J filters respectively. (Straatman et al. 2016). Star-forming galaxies are selected by taking the inverse of the quiescent galaxy mask.

$$\begin{aligned} U - V &> 1.3, \\ V - J &< 1.6, \\ U - V &> 0.88 \times (V - J) + 0.59 \end{aligned} \quad (1)$$

2.3. Bolometric IR Luminosity Derivation

The bolometric IR luminosity is defined and calculated by integrating under the best-fit SED of each source from $8\text{-}1000\mu\text{m}$. Specifically, the averaged Wuylts et al. (2008) template is used to fit the $24\text{-}160\mu\text{m}$ photometry and the total $8\text{-}1000\mu\text{m}$ bolometric IR luminosity is then estimated from the best fit. Refer to section 6 of Straatman et al. (2016) for a full description of the bolometric IR luminosity calculation. We use the bolometric IR luminosities to calculate the bolometric IR luminosity function of the ZFOURGE survey up to $z \approx 6$ (see section 4)

The $24\mu\text{m}$ flux is usually a good proxy for the bolometric flux (Rodighiero et al. 2010). However, when the $24\mu\text{m}$ flux limit is used with the ZFOURGE bolometric luminosity, the limit varies with redshift, possibly due to spectral features shifting in and out of the template fitting process. Instead, we calculate the bolometric flux from the bolometric luminosity and take the 80% completeness as the flux limit. We calculate the ZFOURGE bolometric flux limit to be $3.882 \times 10^{-18} \text{ W/m}^2$. The ZFOURGE star-forming and quiescent dominated sources have very similar flux limits. The CIGALE total and star-forming sources have a flux limit of $5.232 \times 10^{-18} \text{ W/m}^2$. The CIGALE AGN flux also varies with redshift, so we calculate the 80% completeness for each redshift bin individually. Additionally, luminosity completeness limits for ZFOURGE and CIGALE are calculated for each redshift bin and are defined as the minimum luminosity that a galaxy must have for it's maximum distance to be located at the end of the redshift bin.

3. CIGALE

CIGALE (Code Investigating GALaxy Emission) (Boquien et al. 2019) is a versatile software package designed to model the spectral energy distributions (SEDs) of galaxies. It uses a modular approach to create models that account for various physical processes in galaxies. These processes include star formation history, stellar population synthesis, nebular emission, dust attenuation, and dust emission. CIGALE also includes the capability to model the emission from active galactic nuclei (AGN) and incorporates the effects of the intergalactic medium. This flexibility makes CIGALE a powerful tool for investigating galaxy evolution and the

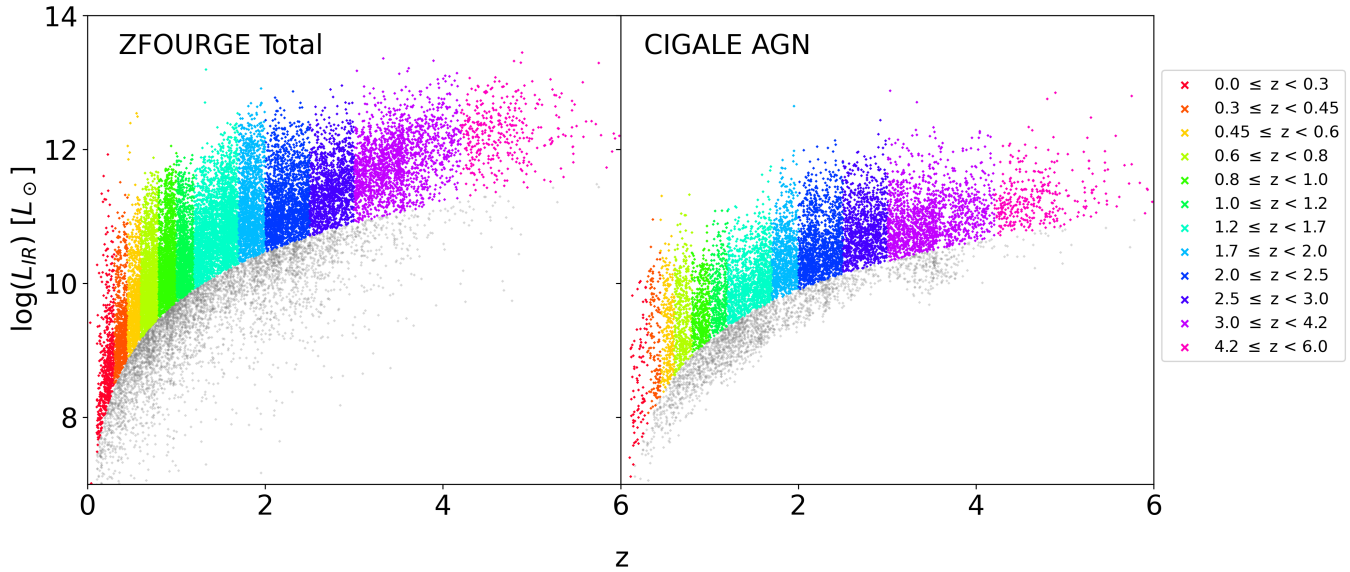


Figure 1: Luminosity-redshift distributions of (left) the ZFOURGE bolometric 8 – 1000 μ m luminosity and (right) the CIGALE AGN total luminosity. Sources are coloured by redshift bin. ZFOURGE sources are removed (coloured grey) based on an 80% completeness cut of the bolometric flux. CIGALE AGN sources are removed based on an 80% completeness cut of the bolometric flux in each redshift bin.

interplay between different galactic components. (Boquien et al. 2019).

[example SED here.](#)

3.1. SED Decomposition

Ollie description of SED decomposition

4. Luminosity Functions

Galaxy luminosity functions (LF) are statistical distributions that describe the spatial density of galaxies at different luminosities and are a fundamental tool for quantifying their evolution across cosmic time scales (Han et al. 2012; Dai et al. 2009; Wylezalek et al. 2014).

By splitting the data into redshift bins, an accurate picture of galaxy distribution and evolution is acquired. The differences in the bins provide insight into how galaxies have evolved through time and point to periods of increased or decreased activity. ZFOURGE allows us to look at the infrared (IR) LF of galaxies with increased depth, extending the LF to potentially redshift of $z \approx 6$.

4.1. V_{max}

To estimate the luminosity function from our data, we utilise the $1/V_{max}$ method (Schmidt 1968). The $1/V_{max}$ method does not make any assumptions or depend on the shape of the luminosity function itself, making this method a very reliable model of the LF shape. The $1/V_{max}$ method accounts for the maximum observable volume of each galaxy and is given by equation 2.

$$\phi(L, z) = \frac{1}{\Delta \log L} \sum_{i=1}^N \frac{1}{V_{max,i}} \quad (2)$$

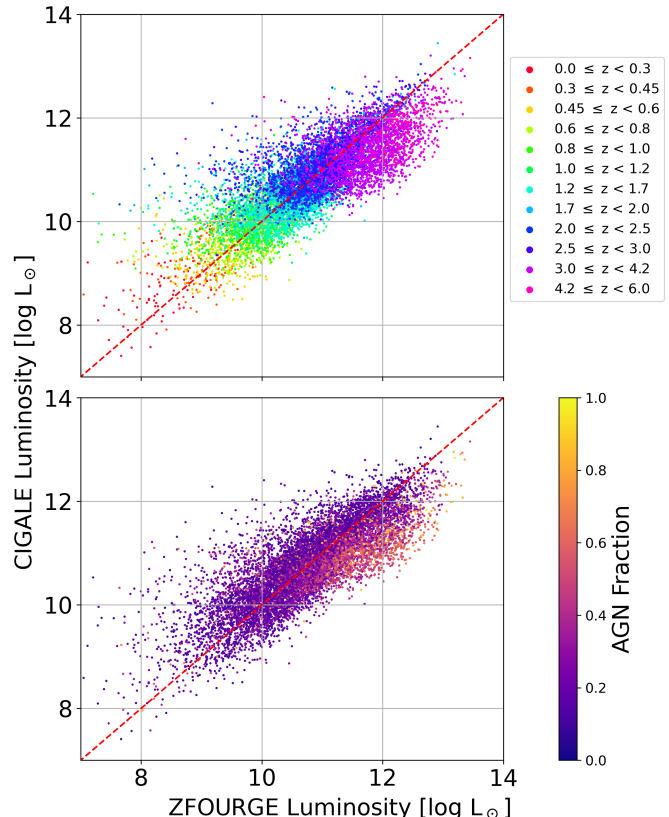


Figure 2: ZFOURGE bolometric 8-1000 μ m IR luminosity compared to CIGALE total luminosity. Top: Sources coloured by redshift bin. Bottom: sources coloured by AGN fraction (F_{AGN}). AGN fraction clearly increases with redshift. At $z \geq 3$ the average AGN fraction is greater than 30%.

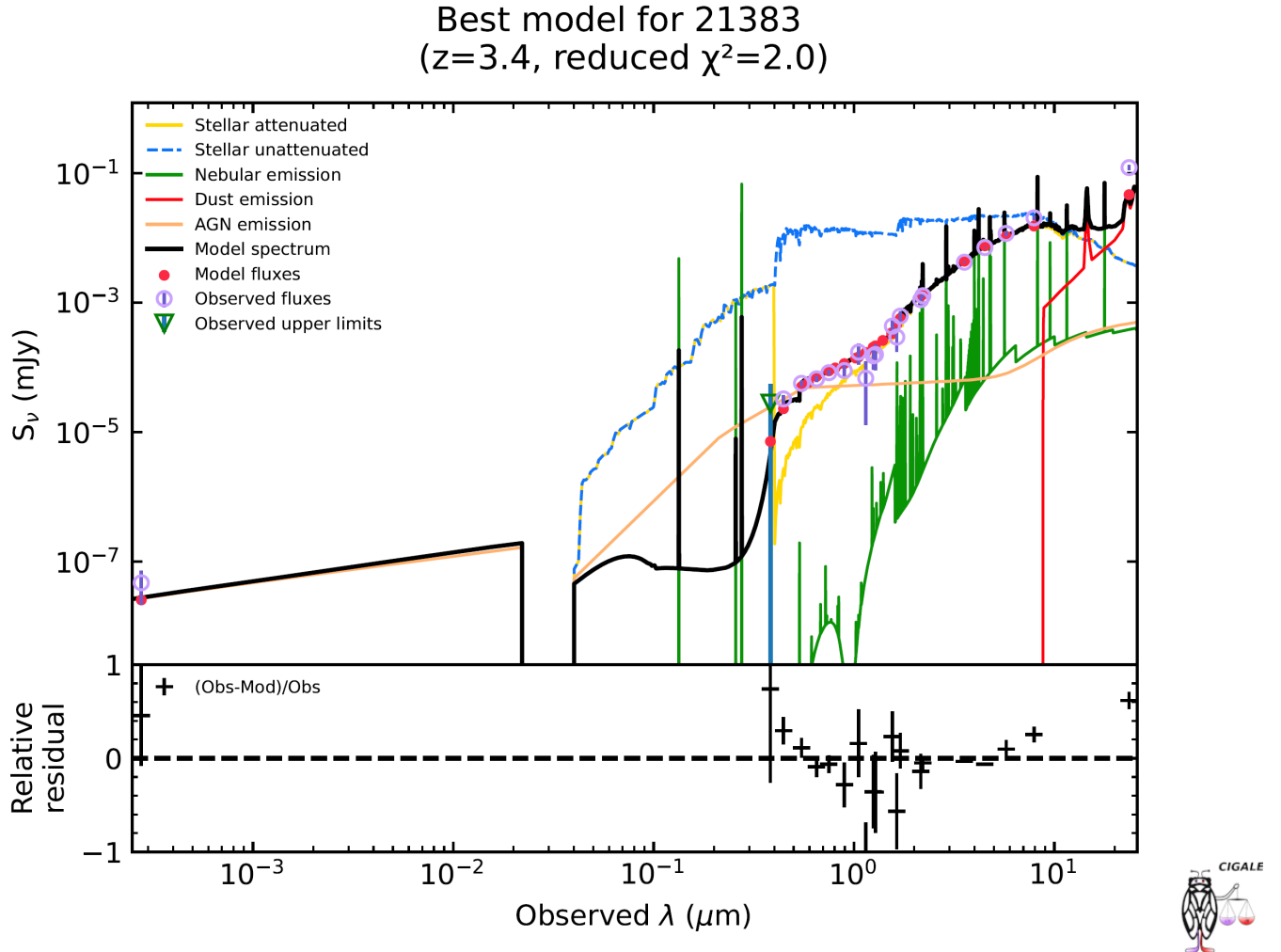


Figure 3: Example SED of different galactic components.

where V_{max} represents the maximum co-moving volume of the i -th source and $\Delta \log(L)$ is the width of the luminosity bin. In practice, to observe the evolution of the luminosity function through cosmic time, the maximum observable volume (V_{max}) is calculated for each redshift bin where the volume is limited by the upper and lower bounds of the redshift bin. For example, galaxies above $10^{12} L_\odot$ appearing in the first redshift bin $0.00 \leq z < 0.30$ have a maximum distance and volume corresponding to $z = 0.30$, even though such galaxies could potentially be detected up to $z = 4$ with the same flux limit. Additionally, redshift bins are split into luminosity bins to observe the number density evolution across the different classes of luminosity such as LIRGS ($10^{11} < L_{IR} < 10^{12} L_\odot$) and ULIRGS ($L_{IR} > 10^{12} L_\odot$). V_{max} of each galaxy is calculated by taking the maximum comoving-volume of the redshift bin the galaxy resides in and subtracting the comoving-volume at the beginning of the redshift bin (equation 2). We account for the survey area probed by ZFOURGE (0.1111 degrees²) which normalises the volume probed across the whole sky (41,253 degrees²).

$$V_{max,i} = \frac{4}{3}\pi (D_{max}^3 - D_{min}^3) \times \frac{A}{41,253} \quad (3)$$

Since all sources with maximum distances smaller than the end of the redshift bin are removed, the volume probed for a galaxy

in a redshift bin is the same for all galaxies in the same redshift bin. Different redshift bins have different volumes and each luminosity bin has a different number density ϕ . Therefore, D_{min} and D_{max} are the comoving-distances at the beginning and end of the redshift bin respectively. We calculate D_{max} and D_{min} using `astropy.cosmology.FlatLambdaCDM.comoving_distance` (Astropy Collaboration et al. 2022) for all sources in each redshift bin above the luminosity-completeness limits. We limit each luminosity bin to a minimum of 5 sources, or else the luminosity bin is discarded. The relative LF number density 1σ error values are calculated with:

$$\phi(L, z) = \frac{1}{\Delta \log L} \sqrt{\sum_i \frac{1}{V_{max}^2}} \quad (4)$$

4.2. Fitting Functions

To model LFs, one of the most widely used methods is the Schechter function (Schechter 1976) (equation 5). This function is beneficial for describing the LF of galaxies because it can represent observed features such as a power-law decline at the faint end and an exponential cutoff at the bright end.

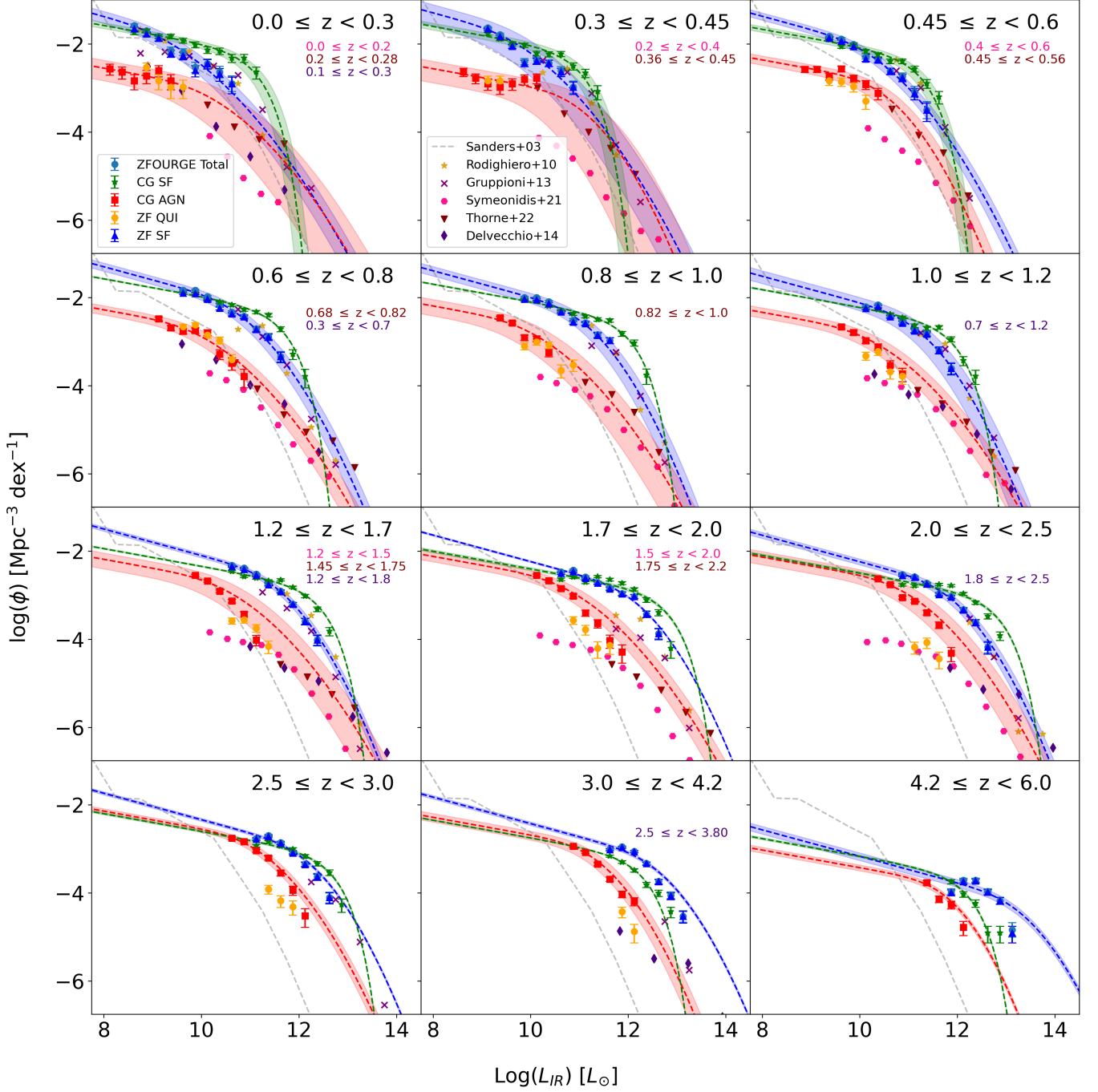


Figure 4: The luminosity functions of major galaxy populations in ZFOURGE and CIGALE calculated using the Vmax method. The ZFOURGE bolometric IR ($8-1000\mu\text{m}$) LF are presented by the light blue circular data points. Dark blue circle points represent the LF of the ZFOURGE star-forming population. Orange circle points are the ZFOURGE quiescent population. The CIGALE star-forming and AGN LFs are given as the green stars and red squares respectively. The blue and red dashed lines show the best fit Saunders function (Saunders et al. 1990) to the ZFOURGE total and CIGALE AGN LF respectively. The green dashed line shows the best fit Schechter function (Schechter 1976) to the CIGALE SF LF. The shaded regions represent the 1σ functional fit errors. The luminosity completeness limit of each redshift bin is where we stop displaying fainter ϕ values. Where possible, comparable literature results are also shown. The local Sanders et al. (2003) luminosity function is shown across all redshift bins as the grey dashed line. Rodighiero et al. (2010) is shown as gold filled stars from $0 < z < 2.5$. Gruppioni et al. (2013) is shown as purple crosses from $0 < z < 4.2$. Symeonidis & Page (2021) AGN are shown as the pink hexagons. Thorne et al. (2022) AGN are shown as the maroon upside down triangles. Delvecchio et al. (2014) AGN as indigo diamonds. Differing redshift bins are colour labelled accordingly. Our ZFOURGE total results are consistent with various sources across redshift bins in the literature (Fu et al. 2010; Caputi et al. 2007; Huang et al. 2007)

Table 1.: ZFOURGE Low redshift bolometric IR (8-1000 μ m) LF ϕ values calculated using the 1/Vmax method.

$\log_{10}(L_{IR}/L_\odot)$	$0.00 \leq z < 0.30$	$0.30 \leq z < 0.45$	$0.45 \leq z < 0.60$	$0.60 \leq z < 0.80$	$0.80 \leq z < 1.00$	$1.00 \leq z < 1.20$
8.50 – 8.75	-1.58 ± 0.04	-	-	-	-	-
8.75 – 9.00	-1.70 ± 0.04	-	-	-	-	-
9.00 – 9.25	-1.83 ± 0.05	-1.64 ± 0.03	-	-	-	-
9.25 – 9.50	-2.15 ± 0.07	-1.79 ± 0.03	-1.83 ± 0.03	-	-	-
9.50 – 9.75	-2.19 ± 0.08	-2.05 ± 0.05	-1.89 ± 0.03	-1.83 ± 0.02	-	-
9.75 – 10.00	-2.54 ± 0.12	-2.40 ± 0.07	-2.01 ± 0.03	-1.83 ± 0.02	-2.00 ± 0.02	-
10.00 – 10.25	-2.45 ± 0.11	-2.38 ± 0.07	-2.30 ± 0.05	-1.98 ± 0.02	-2.00 ± 0.02	-2.21 ± 0.03
10.25 – 10.50	-2.64 ± 0.13	-2.44 ± 0.07	-2.37 ± 0.05	-2.17 ± 0.03	-2.09 ± 0.02	-2.17 ± 0.02
10.50 – 10.75	-2.90 ± 0.18	-2.60 ± 0.09	-2.62 ± 0.07	-2.34 ± 0.04	-2.31 ± 0.03	-2.41 ± 0.03
10.75 – 11.00	-	-2.98 ± 0.14	-2.74 ± 0.08	-2.43 ± 0.04	-2.52 ± 0.04	-2.56 ± 0.04
11.00 – 11.25	-	-	-3.09 ± 0.12	-2.71 ± 0.06	-2.58 ± 0.04	-2.75 ± 0.05
11.25 – 11.50	-	-	-3.50 ± 0.19	-2.89 ± 0.07	-2.85 ± 0.06	-2.82 ± 0.05
11.50 – 11.75	-	-	-	-3.34 ± 0.12	-2.98 ± 0.07	-3.20 ± 0.08
11.75 – 12.00	-	-	-	-	-	-3.61 ± 0.13

Note: Luminosity bin ϕ values are centred.

Table 2.: ZFOURGE High redshift bolometric IR (8-1000 μ m) LF ϕ values calculated using the 1/Vmax method.

$\log_{10}(L_{IR}/L_\odot)$	$1.20 \leq z < 1.70$	$1.70 \leq z < 2.00$	$2.00 \leq z < 2.50$	$2.50 \leq z < 3.00$	$3.00 \leq z < 4.20$	$4.20 \leq z < 6.00$
10.50 – 10.75	-2.33 ± 0.02	-2.47 ± 0.02	-	-	-	-
10.75 – 11.00	-2.39 ± 0.02	-2.43 ± 0.02	-2.54 ± 0.02	-	-	-
11.00 – 11.25	-2.52 ± 0.02	-2.59 ± 0.03	-2.58 ± 0.02	-2.77 ± 0.03	-	-
11.25 – 11.50	-2.75 ± 0.03	-2.71 ± 0.03	-2.73 ± 0.02	-2.70 ± 0.02	-	-
11.50 – 11.75	-2.91 ± 0.03	-2.84 ± 0.04	-2.97 ± 0.03	-2.86 ± 0.03	-3.02 ± 0.02	-
11.75 – 12.00	-3.21 ± 0.05	-2.96 ± 0.04	-3.03 ± 0.03	-3.07 ± 0.04	-2.96 ± 0.02	-3.97 ± 0.06
12.00 – 12.25	-3.59 ± 0.07	-3.03 ± 0.05	-3.33 ± 0.05	-3.35 ± 0.05	-3.06 ± 0.02	-3.71 ± 0.05
12.25 – 12.50	-4.02 ± 0.12	-3.43 ± 0.07	-3.62 ± 0.07	-3.63 ± 0.07	-3.33 ± 0.03	-3.71 ± 0.04
12.50 – 12.75	-	-3.87 ± 0.12	-4.18 ± 0.13	-4.11 ± 0.12	-3.74 ± 0.05	-3.97 ± 0.06
12.75 – 13.00	-	-	-	-	-4.06 ± 0.08	-4.18 ± 0.08
13.00 – 13.25	-	-	-	-	-4.53 ± 0.13	-4.84 ± 0.16

Note: Luminosity bin ϕ values are centred.



$$\phi(L) = \phi^* \left(\frac{L}{L^*} \right)^{1-\alpha} \exp \left(-\frac{L}{L^*} \right) \quad (5)$$

Where $\phi(L)$ is the number of galaxies per unit volume (number density), ϕ^* is the characteristic normalisation factor, L is the bolometric IR (8-1000 μ m) luminosity, L^* is the characteristic luminosity, and α is the faint end slope (Schechter 1976). The Schechter function, however, is not the only commonly used fitting function at mid- and far-IR wavelengths. The bright end slope of the Schechter function cannot be independently varied to better fit a dataset. We make use of a modified Schechter function known as the Saunders function (Saunders et al. 1990) (equation 6) to fit our luminosity function data points.

$$\phi(L) = \phi^* \left(\frac{L}{L^*} \right)^{1-\alpha} \exp \left[-\frac{1}{2\sigma^2} \log_{10}^2 \left(1 + \frac{L}{L^*} \right) \right] \quad (6)$$

Where the parameters are the same as the Schechter function (equation 5), but with the introduction of σ to vary the bright end slope. Our deep ZFOURGE data probes to fainter luminosities across all redshift bins, thus better constraining the faint end of the LF. However, we lack data at the brighter luminosities. At our lowest redshift bins, we do not have comparatively high luminosity bins to fit the bright end of the luminosity function. We tested both Schechter and Saunders functional fits, finding that the Saunders function fits our data better. We fix σ with values matching the bright end of the literature (see section 5.2 for a discussion on parameter evolution). We opt to fix $\alpha = 1.3$ for our Saunders fits and leave L^* and ϕ^* as free parameters. The evolution of L^* and ϕ^* will be discussed in section 5.2 where we show the evolution in figure 6 and values in tables 5 and 6 for ZFOURGE and CIGALE respectively.

We use `scipy.optimize.curve_fit` (Virtanen et al. 2020) to perform the fitting and calculate 1 σ relative parameter dispersion

Table 3.: CIGALE low-redshift AGN LF ϕ values calculated using the 1/Vmax method.

$\log_{10}(L_{IR}/L_\odot)$	$0.00 \leq z < 0.30$	$0.30 \leq z < 0.45$	$0.45 \leq z < 0.60$	$0.60 \leq z < 0.80$	$0.80 \leq z < 1.00$	$1.00 \leq z < 1.20$
8.00 – 8.25	-2.57 ± 0.12	-	-	-	-	-
8.25 – 8.50	-2.64 ± 0.13	-	-	-	-	-
8.50 – 8.75	-2.84 ± 0.16	-2.64 ± 0.09	-	-	-	-
8.75 – 9.00	-2.74 ± 0.14	-2.78 ± 0.11	-2.58 ± 0.07	-	-	-
9.00 – 9.25	-2.60 ± 0.13	-2.90 ± 0.13	-2.58 ± 0.07	-2.48 ± 0.04	-	-
9.25 – 9.50	-2.84 ± 0.16	-2.98 ± 0.14	-2.74 ± 0.08	-2.69 ± 0.05	-2.46 ± 0.04	-
9.50 – 9.75	-	-2.90 ± 0.13	-2.57 ± 0.07	-2.76 ± 0.06	-2.58 ± 0.04	-2.67 ± 0.04
9.75 – 10.00	-	-2.81 ± 0.11	-2.79 ± 0.09	-2.75 ± 0.06	-2.91 ± 0.06	-2.79 ± 0.05
10.00 – 10.25	-	-2.78 ± 0.11	-2.92 ± 0.10	-2.80 ± 0.06	-2.94 ± 0.06	-2.98 ± 0.06
10.25 – 10.50	-	-	-3.12 ± 0.13	-3.28 ± 0.11	-3.25 ± 0.09	-3.12 ± 0.07
10.50 – 10.75	-	-	-	-3.49 ± 0.14	-	-3.54 ± 0.12
10.75 – 11.00	-	-	-	-3.79 ± 0.19	-	-3.73 ± 0.14

Note: Luminosity bin ϕ values are centred.

Table 4.: CIGALE high-redshift AGN LF ϕ values calculated using the 1/Vmax method.

$\log_{10}(L_{IR}/L_\odot)$	$1.20 \leq z < 1.70$	$1.70 \leq z < 2.00$	$2.00 \leq z < 2.50$	$2.50 \leq z < 3.00$	$3.00 \leq z < 4.20$	$4.20 \leq z < 6.00$
9.75 – 10.00	-2.55 ± 0.02	-	-	-	-	-
10.00 – 10.25	-2.68 ± 0.02	-2.55 ± 0.03	-	-	-	-
10.25 – 10.50	-2.91 ± 0.03	-2.67 ± 0.03	-2.63 ± 0.02	-	-	-
10.50 – 10.75	-3.13 ± 0.04	-2.85 ± 0.04	-2.76 ± 0.03	-2.76 ± 0.03	-	-
10.75 – 11.00	-3.43 ± 0.06	-3.02 ± 0.05	-3.06 ± 0.04	-2.84 ± 0.03	-2.94 ± 0.02	-
11.00 – 11.25	-4.02 ± 0.12	-3.40 ± 0.07	-3.13 ± 0.04	-3.04 ± 0.04	-3.08 ± 0.02	-
11.25 – 11.50	-	-3.64 ± 0.09	-3.39 ± 0.05	-3.21 ± 0.04	-3.35 ± 0.03	-3.77 ± 0.05
11.50 – 11.75	-	-4.03 ± 0.14	-3.68 ± 0.07	-3.55 ± 0.06	-3.69 ± 0.05	-4.14 ± 0.07
11.75 – 12.00	-	-4.29 ± 0.19	-4.32 ± 0.15	-3.94 ± 0.10	-4.03 ± 0.07	-4.27 ± 0.09
12.00 – 12.25	-	-	-	-4.52 ± 0.19	-4.19 ± 0.09	-4.78 ± 0.15

Note: Luminosity bin ϕ values are centred.

errors (shown as the shaded region in figure 4) using the equation: $perr = np.sqrt(np.diag(pcov))$. $perr$ relates the covariance of each individual fit; all redshift bins in figure 4 show a fit error, but in some, the covariance is very small. Parameter errors can be found in tables 5 and 6.

5. Discussion

5.1. Bolometric IR LF

We calculate and compare the luminosity function of ZFOURGE total and UVJ split galaxies with CIGALE decomposed star-forming and AGN luminosity functions across twelve redshift bins from $0 \leq z < 6$ in figure 4. We fit the Saunders' function (Saunders et al. 1990) (equation 6) in blue using `scipy.optimize.curve_fit` (Virtanen et al. 2020) and calculate 1σ uncertainties on the parameter covariance using `np.sqrt(np.diag(pcov))` (Harris et al. 2020).



For the ZFOURGE data, we compare our results with Rodighiero et al. (2010) across redshift bins from $0 \leq z < 2.5$ as gold stars and Gruppioni et al. (2013) as purple crosses from $0 \leq z < 4.2$. We also compare our results with Fu et al. (2010); Huang et al. (2007); Caputi et al. (2007) but choose not to clutter our LF (4) with disjointed redshift bins from the literature and instead compare locally. Across all redshift bins (except the most local), we consistently see that the ZFOURGE ϕ values in blue extend much fainter than the rest of the literature, showcasing ZFOURGE's ability to probe to fainter luminosities. However, there is still room to improve constraints at the faint end of the (ZFOURGE) galaxy LF. At lower redshifts ($0.00 \leq z < 1.20$), probing an order of magnitude fainter in each redshift bin in $\log(L_{IR}/L_\odot)$ space would be sufficient to well-constrain the faint end of the LF. At higher redshifts ($z \geq 1.20$), probing two orders fainter in each redshift is required to better constrain the faint end slope of the (ZFOURGE) galaxy LF.

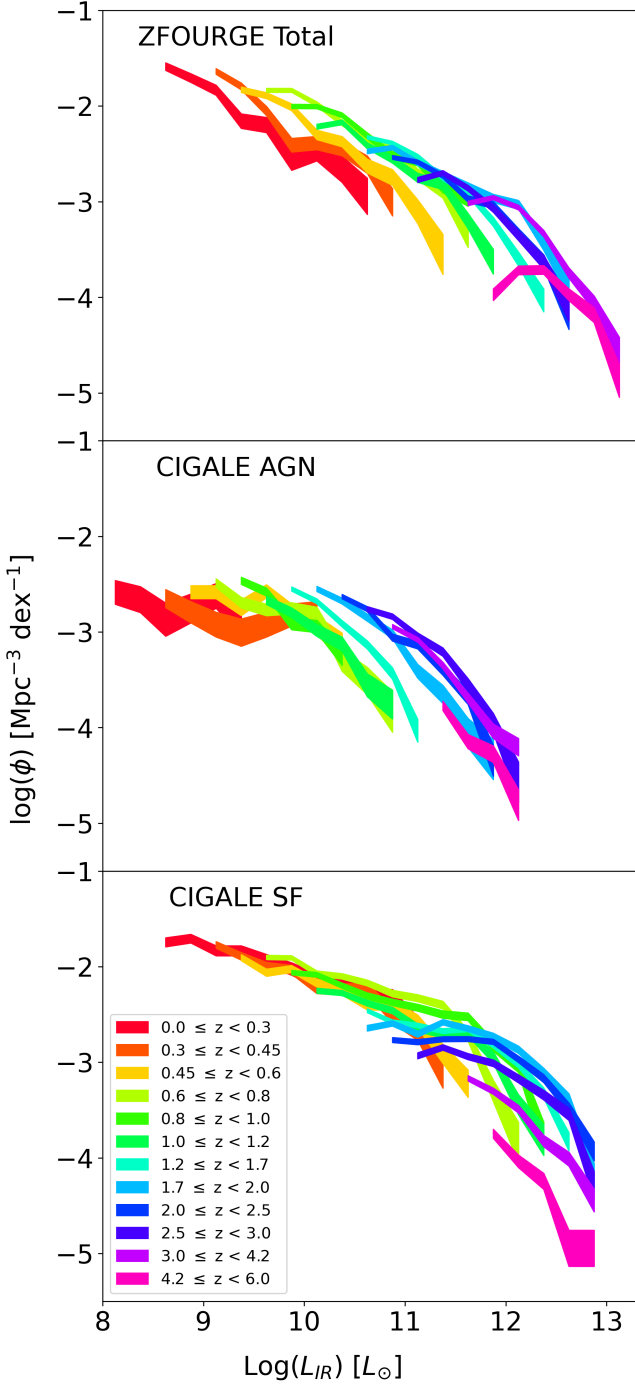


Figure 5: Combined evolution of the ZFOURGE total (top), CIGALE AGN (middle), and CIGALE SF (bottom) luminosity functions shown in figure 4. The redshift evolution of each binned LF is easier to visualise. Data points are shaded between the 1σ uncertainties and coloured by redshift bin.

There is very good agreement with the ZFOURGE total results from the literature in all bins except $1.7 \leq z < 2$ and $3.0 \leq z < 4.2$. In these redshift bins, ZFOURGE results show ϕ values ≈ 0.5 dex higher across all luminosity bins when compared to the literature (Gruppioni et al. 2013; Rodighiero et al. 2010). We posit that ZFOURGE is detecting fainter sources in these redshift bins than has been previously observed. From $1.7 \leq z < 2$, both Rodighiero

et al. (2010) and Gruppioni et al. (2013) show a large drop in their faintest luminosity bins, consistent with incompleteness. Gruppioni et al. (2013) sees a drop of $\approx 0.5 \log(\phi_*)$ or more in each luminosity bin of the $3.0 \leq z < 4.2$ LF when compared to their previous redshift bin and is very likely to be solely an incompleteness issue given it is their final redshift bin. The fact that both Gruppioni et al. (2013) and Rodighiero et al. (2010) see a drop from $1.7 \leq z < 2$ is very interesting. Curiously, this does not seem to be a problem for either in their neighbouring redshift bins, or any other redshift bin for that matter. Rodighiero et al. (2010) utilises multiwavelength Spitzer observations whereas Gruppioni et al. (2013) uses Herschel/PACS data to estimate the total IR LF. Given that this incompleteness exists across multiple surveys and instruments, it remains to be seen why a drop in the $1.7 \leq z < 2$ redshift bin exists at all when neighbouring redshift bins show no sign of incompleteness.

Similar can be said about our final redshift bin $4.2 \leq z < 6.0$ (figure 4). We have six luminosity bins in this redshift range that show a significant drop along the faint end slope of our LF. This is a sign of incompleteness, and indeed a turnover is present. Thus, the redshift bin $4.2 \leq z < 6.0$ is incomplete and should be taken as a lower limit.

In figure 5 we show the combined evolution of the ZFOURGE bolometric IR (8–1000 μ m) LF. The LF is filled between the 1σ uncertainty calculated using equation 4. With this plot, it is easier to see the evolution of the LF across luminosity and redshift. There is a clear downwards density trend seen with increasing luminosity and redshift. This result is significant because it highlights the fact that [where we going with this?](#) As redshift increases, the luminosity function indeed decreases. Again, our redshift bin $4.2 \leq z < 6.0$ is incomplete and should be taken as a lowest limit. Nevertheless, the downwards evolutionary trend is still observed.

For the CIGALE AGN, we compare our results with Symeonidis & Page (2021) from $0 \leq z < 2.5$ as pink hexagons and Thorne et al. (2022) from $0 \leq z < \approx 2$. Symeonidis & Page (2021) derives their IR AGN ϕ values from the hard X-ray LFs by Aird et al. (2015). Thorne et al. (2022), who performs very similar work to us, uses the SED fitting code ProSpect (Robotham et al. 2020; Leja et al. 2017) to decompose the bolometric IR LF to isolate and subsequently estimate the AGN LF. We fit the Saunders' function (Saunders et al. 1990) (equation 6) in red and 1σ uncertainties to our CIGALE decomposed AGN LF. We include Thorne et al. (2022) AGN in our fitting process as we do not have comparatively bright AGN to constrain the bright end of the luminosity function.

In the first few redshift bins from $0 \leq z < 0.8$, our CIGALE AGN LF results and Saunders' function fits are broadly consistent with the results in the literature. At higher redshifts and fainter luminosities, the literature LFs flatten out substantially. Comparatively, our CIGALE AGN LFs do not flatten at all and instead continue to rise. With CIGALE we are able to decompose and isolate the AGN contribution to luminosities as faint as $10^8 L_\odot$. Importantly, we are able to probe fainter than Thorne et al. (2022) whose faintest luminosity bin is never less than $10^{10} L_\odot$ (accounting for completeness limits) with their ProSpect AGN. Our CIGALE AGN LFs lack ϕ values at the brighter end of the luminosity function, requiring us to use Thorne et al. (2022) ϕ values to constrain our Saunders function fits.

Because the Symeonidis & Page (2021) AGN are derived from the hard X-ray LF in Aird et al. (2015) who do not include Compton-thick AGN, the flattening at fainter luminosities is most likely due to X-ray emission not identifying the highly obscured

faint AGN population which SED fitting allows us to recover (Thorne et al. 2022; Gruppioni et al. 2011; Brown et al. 2019). Not plotted in figure 4 are type-1 and type-2 AGN added together from Symeonidis & Page (2021). This is because they appear in only some redshift bins and in at most three luminosity bins each. However, these combined AGN are mostly elevated above their IR AGN, especially from $1.2 \leq z < 2.5$. Our AGN LF ϕ values and functional fits are therefore consistent with the literature. CIGALE is able to extend the AGN LF to fainter luminosities that have never been probed before.

As the CIGALE AGN LF evolves with redshift, the faint end approaches ($0 \leq z < 2.5$) and almost takes over ($z > 2.5$) the number density values of the CIGALE SF LF. It is well understood that the SF fraction of galaxies decreases as redshift and L_{IR} increases (Wu et al. 2011). AGN fraction increases with redshift and L_{IR} (Symeonidis & Page 2021; Thorne et al. (2022) and references within). Although our results do not show the number densities of AGN overtaking star-forming galaxies, it is probable that future work probing higher redshifts will.

As is seen in figure 4 (especially in the lower redshift bins), the CIGALE star-forming LF is elevated above the ZFOURGE total, star-forming, and comparable literature LFs at brighter luminosities. Towards fainter luminosities we see very good agreement between the CIGALE SF and ZFOURGE LFs. There are potentially many factors that could produce this result. Work by Wu et al. (2011) has shown that the UV and optical wavelengths closely follow a Schechter function. In contrast, the IR wavelengths have a shallower exponential which is inconsistent with a Schechter function (Symeonidis & Page 2019). Fu et al. (2010) proposed that this difference is due to the AGN contribution to the IR Galaxy LF. Wu et al. (2011) also concludes that by removing AGN, the bright end slope is consistent with a Schechter function. We argue that CIGALE is not overestimating the star-forming fraction of galaxy light and is able to accurately eliminate AGN contamination. Although our results in figure 4 show that we do not have many luminosity bins along the bright end, there are enough to constrain a well defined Schechter functional fit.

The bright end slope of a Schechter function is, as expected, too steep to accurately describe the ZFOURGE total IR LF (Wu et al. 2011), in agreement with the literature (Rodighiero et al. 2010; Gruppioni et al. 2013; Symeonidis & Page 2019). Even after removing AGN identified galaxies (552, Cowley et al. (2016)), our ZFOURGE star-forming luminosity functions do not show an improved Schechter function fit as predicted by Fu et al. (2010); Wu et al. (2011). The most likely reason is that Cowley et al. (2016) only identifies the most AGN dominated sources and is not able to identify low-luminosity AGN. AGN and star-formation is tightly coupled (cite) with both AGN activity and star-formation likely happening at the same time or in offset cycles (cite). At higher redshifts ($z > 2$), it becomes increasingly important to disentangle AGN and star-forming components of galaxy emission to accurately model the evolution of both.

5.2. Parameter Evolution

In this section, we discuss the parameter evolution of the Saunders and Schechter luminosity function fits in figure 4. The evolution of ϕ^* and L^* across redshift is presented in figure 6 with values and 1σ errors in tables 5, 6, and 7. The best fitting parameter values were calculated using `scipy.optimize.curve_fit` (Virtanen et al. 2020) and 1σ parameter uncertainties are calculated using `perr = np.sqrt(np.diag(pcov))` (Harris et al. 2020) which

relates the covariance of the best fit parameters. As discussed in section 5.1, our final redshift bin suffers from incompleteness. Our 1σ errors are largest in the lowest redshift bins; ZFOURGE is better suited for probing higher redshifts.

As ZFOURGE is able to probe fainter luminosities, we are able to better constrain the faint end slope of the luminosity function, which we do by fixing $\alpha = 1.3$ across all bins of the ZFOURGE total LF. This result differs from the literature where Rodighiero et al. (2010); Gruppioni et al. (2013) fix $\alpha = 1.2$ whereas Fu et al. (2010) leaves α as a free fitting parameter found to be $\alpha = 1.46$ (respective to our Saunders' fitting function). As we lack luminosity bins along the bright end of the LF, we fix the bright end σ to values which fit best to the literature if the fits were poor. The CIGALE SF LF is fit with a Schechter function with a faint end slope of $\alpha = 1.2$ as the faint end rises shallower than the ZF total. The CIGALE SF LF is fit with a Saunders function also with a faint end slope of $\alpha = 1.2$. Bright end luminosity bins are missing, so we include the datapoints of Thorne et al. (2022) to help constrain the fitting process. However, we still fix σ to values that closely follow the literature.

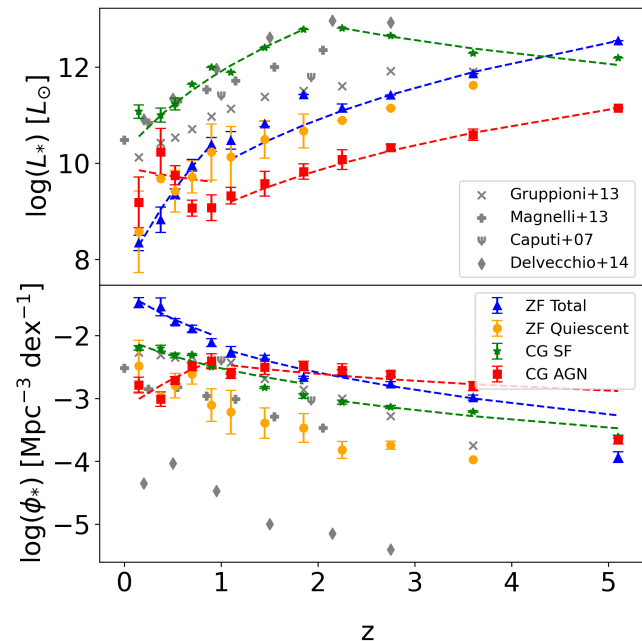


Figure 6: Best fitting parameters and 1σ uncertainties to our luminosity functions. Top: L^* evolution. Bottom: ϕ^* evolution. Blue triangles represent the ZFOURGE total and orange circles the ZFOURGE quiescent population. Red squares represent the CIGALE AGN and green crosses the CIGALE star-forming population. Dashed lines represent the $\propto (1+z)^k$ evolution. We compare our results to the relevant literature coloured gray. Gruppioni et al. (2013) crosses, Magnelli et al. (2013) pluses, and Caputi et al. (2007) uppercase Psi's.

Our ZFOURGE free L^* and ϕ^* parameters are found to evolve differently than is present in the literature. However, our fitting process is robust (Virtanen et al. 2020), and the evolution of the free parameters does not change significantly when the fixed parameters are altered. There is also the matter of degeneracy between L^* and ϕ^* . A decrease in L^* can be somewhat compensated for by an increase in ϕ^* and vice-versa. Thus, the absolute

Table 5. : ZFOURGE Total Saunders parameter evolution values as a function of redshift

z	$\log(L^*)$	$\log(\phi^*)$	α	σ
$0.00 \leq z < 0.30$	8.34 ± 0.16	-1.48 ± 0.08	1.3	1.1
$0.30 \leq z < 0.45$	8.82 ± 0.26	-1.54 ± 0.14	1.3	1.0
$0.45 \leq z < 0.60$	9.36 ± 0.10	-1.78 ± 0.05	1.3	0.9
$0.60 \leq z < 0.80$	9.96 ± 0.12	-1.89 ± 0.05	1.3	0.8
$0.80 \leq z < 1.00$	10.39 ± 0.14	-2.11 ± 0.06	1.3	0.7
$1.00 \leq z < 1.20$	10.47 ± 0.18	-2.26 ± 0.09	1.3	0.7
$1.20 \leq z < 1.70$	10.82 ± 0.06	-2.35 ± 0.03	1.3	0.7
$1.70 \leq z < 2.00$	11.42 ± 0.00	-2.67 ± 0.02	1.3	0.7
$2.00 \leq z < 2.50$	11.14 ± 0.08	-2.58 ± 0.04	1.3	0.7
$2.50 \leq z < 3.00$	11.42 ± 0.00	-2.77 ± 0.03	1.3	0.7
$3.00 \leq z < 4.20$	11.86 ± 0.00	-2.99 ± 0.04	1.3	0.7
$4.20 \leq z < 6.00$	12.54 ± 0.00	-3.93 ± 0.08	1.3	0.7

Table 6. : CIGALE AGN Saunders parameter evolution values as a function of redshift

z	$\log(L^*)$	$\log(\phi^*)$	α	σ
$0.00 \leq z < 0.30$	9.19 ± 0.53	-2.79 ± 0.13	1.2	1.0
$0.30 \leq z < 0.45$	9.99 ± 0.59	-2.96 ± 0.14	1.2	1.0
$0.45 \leq z < 0.60$	9.42 ± 0.26	-2.65 ± 0.08	1.2	1.0
$0.60 \leq z < 0.80$	9.07 ± 0.17	-2.49 ± 0.07	1.2	1.0
$0.80 \leq z < 1.00$	9.07 ± 0.27	-2.41 ± 0.12	1.2	1.0
$1.00 \leq z < 1.20$	9.32 ± 0.17	-2.60 ± 0.08	1.2	1.0
$1.20 \leq z < 1.70$	9.57 ± 0.26	-2.50 ± 0.12	1.2	1.0
$1.70 \leq z < 2.00$	9.82 ± 0.16	-2.49 ± 0.07	1.2	1.0
$2.00 \leq z < 2.50$	10.07 ± 0.20	-2.55 ± 0.10	1.2	0.9
$2.50 \leq z < 3.00$	10.32 ± 0.07	-2.61 ± 0.04	1.2	0.8
$3.00 \leq z < 4.20$	10.59 ± 0.12	-2.81 ± 0.07	1.2	0.7
$4.20 \leq z < 6.00$	11.15 ± 0.00	-3.66 ± 0.07	1.2	0.6

values of the parameters themselves can be overlooked in favour of the overall trend in the dataset. The degeneracy between L^* and ϕ^* exists, but the shape of their evolution is consistent across the literature.

We find rapid evolution of ZFOURGE L^* ($L^* = 10^{7.70 \pm 0.14} \times (1+z)^{9.64 \pm 0.51}$ for $z < 1$ and $L^* = 10^{8.37 \pm 0.28} \times (1+z)^{5.31 \pm 0.36}$ for $z > 1$) up to $z \approx 1$ where L^* evolution slows dramatically. ZFOURGE ϕ^* ($\phi^* = 10^{-1.30 \pm 0.07} \times (1+z)^{-2.44 \pm 0.52}$ for $z < 1$ and $\phi^* = 10^{-1.54 \pm 0.12} \times (1+z)^{-2.21 \pm 0.31}$ for $z > 1$) does not show as rapid evolution as L^* at all redshift bins. Compared to the literature, both Gruppioni et al. (2013) and Magnelli et al. (2013) find much shallower L^* evolution from $0 < z < 1$. ZFOURGE evolves 2-3x faster at $0 < z < 1$, but only 1.25x faster at $z > 1$. This could be explained by ZFOURGE probing fainter luminosities, however, ZFOURGE was designed to probe redshifts $z > 1$, and so results at $z < 1$ are not as reliable **is this true?**. And likely something else is going on. From $0 < z < 1$, ZFOURGE characteristic luminosity L^* increases by 134x. From $1 < z < 5$, another 118x

Table 7. : CIGALE SF Schechter parameter evolution values as a function of redshift

z	$\log(L^*)$	$\log(\phi^*)$	α
$0.00 \leq z < 0.30$	11.07 ± 0.14	-2.20 ± 0.04	1.2
$0.30 \leq z < 0.45$	11.00 ± 0.15	-2.20 ± 0.05	1.2
$0.45 \leq z < 0.60$	11.23 ± 0.12	-2.32 ± 0.04	1.2
$0.60 \leq z < 0.80$	11.64 ± 0.00	-2.31 ± 0.01	1.2
$0.80 \leq z < 1.00$	11.99 ± 0.00	-2.50 ± 0.01	1.2
$1.00 \leq z < 1.20$	11.89 ± 0.00	-2.60 ± 0.02	1.2
$1.20 \leq z < 1.70$	12.40 ± 0.00	-2.83 ± 0.02	1.2
$1.70 \leq z < 2.00$	12.78 ± 0.00	-2.96 ± 0.03	1.2
$2.00 \leq z < 2.50$	12.81 ± 0.00	-3.06 ± 0.03	1.2
$2.50 \leq z < 3.00$	12.65 ± 0.00	-3.13 ± 0.02	1.2
$3.00 \leq z < 4.20$	12.29 ± 0.00	-3.21 ± 0.01	1.2
$4.20 \leq z < 6.00$	12.19 ± 0.00	-3.61 ± 0.02	1.2

increase is seen. ZFOURGE ϕ^* decreases by 4x and 47x over the same time period. These redshift ranges represent ≈ 5 Gyrs and ≈ 4 Gyrs of evolution respectively. Thus, ZFOURGE L^* evolution remains roughly constant over the universe's lifetime. ZFOURGE characteristic density ϕ^* shows significant evolution.

The CIGALE SF L^* ($L^* = 10^{10.21 \pm 0.16} \times (1+z)^{5.65 \pm 0.36}$ for $z < 2$ and $L^* = 10^{14.24 \pm 0.25} \times (1+z)^{-2.80 \pm 0.45}$ for $z > 2$) shows slower evolution compared to the ZFOURGE total from $0 < z < 1$ but similar evolution from $1 < z < 2$. In stark contrast to published and ZFOURGE results, the CIGALE SF L^* declines from $z > 2$ onwards. This decline is not seen in the evolution of ϕ^* ($\phi^* = 10^{-2.05 \pm 0.05} \times (1+z)^{-1.58 \pm 0.28}$ for $z < 2$ and $\phi^* = 10^{-2.24 \pm 0.12} \times (1+z)^{-1.58 \pm 0.40}$ for $z > 2$) which has a similar slope across all redshifts and is close to the results published by Magnelli et al. (2013). The reversal in the evolution of L^* above $z > 2$ indicates that star-formation grew from at least $z = 5$ to $z = 2$ and has been declining ever since. It is well known (cite), and hotly debated (cite), that the IR luminosity density has been declining since $z \approx 2$ and we explore this possibility more in section 5.3. CIGALE SF L^* increases by 8x from $0 < z < 1$ and another 8x from $1 < z < 2$. From $2 < z < 5$ L^* decreases by 4x. ϕ^* decreases by 2x, another 2x, and 3.5x over the same period. These redshifts represent 5, 2, and 2 Gyrs of evolution respectively. Gruppioni et al. (2013) and Magnelli et al. (2013) finds similar L^* from $0 < z < 1$ and similar ϕ^* evolution from $0 < z < 2$.

The CIGALE AGN L^* ($L^* = 10^{9.71 \pm 0.53} \times (1+z)^{-1.12 \pm 3.17}$ for $z < 1$ and $L^* = 10^{7.85 \pm 0.11} \times (1+z)^{4.20 \pm 0.15}$ for $z > 1$) and ϕ^* ($\phi^* = 10^{-3.11 \pm 0.16} \times (1+z)^{-2.53 \pm 0.66}$ for $z < 1$ and $\phi^* = 10^{-2.19 \pm 0.20} \times (1+z)^{-0.88 \pm 0.42}$ for $z > 1$) evolve in the opposite direction from the literature and from our ZFOURGE and CIGALE SF parameters at $z < 1$. At $z > 1$, the evolution returns to the normal trend. This could be due to the degeneracy between L^* and ϕ^* as previously mentioned, but such degeneracy has never been so obvious and in such stark contrast to published results. This leaves two possibilities: either CIGALE is able to disentangle the AGN evolution and uncover a significant evolutionary epoch that AGN underwent at $z \approx 1$, or our fitting process and AGN results are biased. The fact that our fitting process produces similar results for the ZFOURGE total as seen in the literature

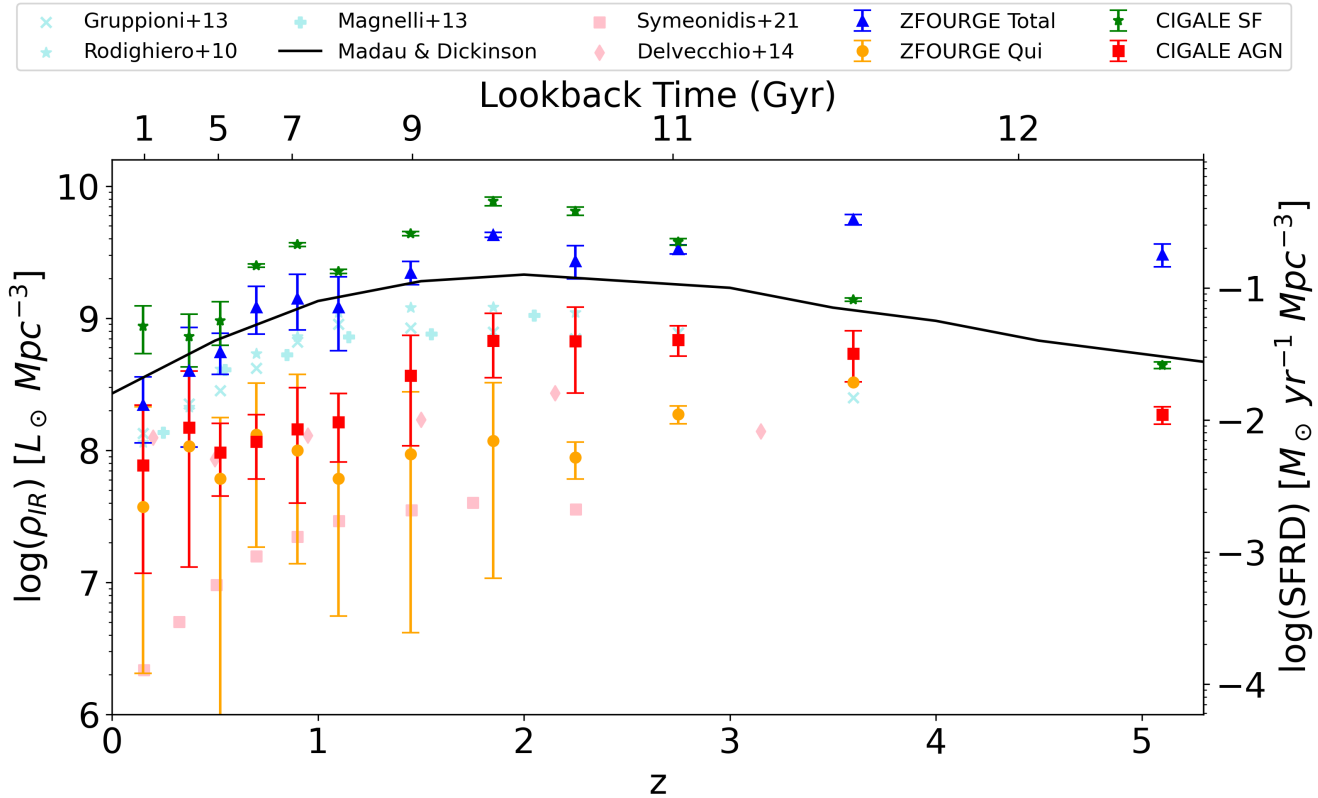


Figure 7: Evolution of the IR luminosity density calculated by integrating under the best fitting functions. 1σ uncertainties are calculated by re-performing the integration with errors from the LF fitting process. Saunders is fit for the ZFOURGE total and CIGALE AGN, whereas Schechter is fit for the CIGALE SF. Blue triangles represent ZFOURGE total, green stars CIGALE SF, and red squares CIGALE AGN. The right side y-axis is obtained from Kennicutt (1998) by dividing ρ_{IR} by $1.7 \times 10^{10} L_\odot$. We compare our results with relevant literature. The top axis shows the lookback time in billions of years. Gruppioni et al. (2013); Rodighiero et al. (2010); Magnelli et al. (2013) as light turquoise compare the total IR luminosity density (with Caputi et al. (2007) similar to the other literature). Symeonidis & Page (2021) and Delvecchio et al. (2014) as pink compare the AGN luminosity density. The solid black line is the Madau & Dickinson (2014) IR ρ_{IR} .

and possibly recovers the turnover in the IR luminosity density for the CIGALE SF gives good evidence to the idea that $z \approx 1$ is a significant epoch for AGN evolution. Delvecchio et al. (2014) and Hopkins et al. (2007) show a similar reversal and subsequent decline in ϕ^* evolution below $z = 1$. However, both do not find a corresponding reversal and uptick in L^* evolution at $z = 1$. CIGALE AGN L^* initially decreases by 1.3x from $0 < z < 1$ and increases by 66x from $1 < z < 5$. AGN ϕ^* increases by 2.4x from $0 < z < 1$ and decreases by 11.4x from $1 < z < 5$.

5.3. Bolometric IR Luminosity Density

We calculate and analyse the IR (8-1000 μ m) luminosity density. Figure 7 shows the IR luminosity density (ρ_{IR}) for ZFOURGE and CIGALE. At each redshift bin, ρ_{IR} is calculated by integrating under the best fitting luminosity function. Schechter (equation 7) is used for the CIGALE SF whereas Saunders (equation 8) is used for ZFOURGE total and CIGALE AGN. We utilise `scipy.integrate.quad` (Virtanen et al. 2020) to perform the integration from 0 to ∞L_\odot by cumulatively summing the integrand at different bounds (e.g. from 10^{10} to $10^{12} L_\odot$, 10^{12} to $10^{14} L_\odot$, etc) because the quadrature algorithm isn't well suited for small

areas over extremely large bounds. In practice, additional calculations of ρ_{IR} above $10^{20} L_\odot$ are negligible. To generate 1σ ρ_{IR} uncertainties, we re-perform the integration using the 1σ LF fit errors.

$$\rho_{IR} = \int_0^\infty \varphi^* \left(\frac{L}{L^*} \right)^{1-\alpha} \exp \left(-\frac{L}{L^*} \right) dL \quad (7)$$

$$\rho_{IR} = \int_0^\infty \varphi^* \left(\frac{L}{L^*} \right)^{1-\alpha} \exp \left[-\frac{1}{2\sigma^2} \log_2^2 \left(1 + \frac{L}{L^*} \right) \right] dL \quad (8)$$

Figure 7 shows the evolution of the IR luminosity density as a function of redshift with our results in table 8. A secondary right-hand-side axis is shown in figure 7 which is a scaling conversion factor to star-formation-rate provided by Kennicutt (1998) calculated by dividing ρ_{IR} by $1.7 \times 10^{10} L_\odot$. We point out that the AGN densities do not have an associated SFR. The top x-axis shows the lookback time in billions of years placing the evolution of the universe in the context of time and showcasing the import evolutionary epochs.

Our ZFOURGE results in figure 7 show rapid evolution from $0 < z < 2$, after which evolution drastically slows down from $z >$

Table 8.: Luminosity density as a function of redshift. Units are in $\log(\rho_{IR}) [L_\odot \text{ Mpc}^{-3}]$. Errors are absolute. ρ_{IR} values are centered on the redshift bin.

z	ZFOURGE Total	CIGALE SF	CIGALE AGN
$0.00 \leq z < 0.30$	$8.34^{0.27}_{0.21}$	$8.94^{0.19}_{0.16}$	$7.89^{0.80}_{0.37}$
$0.30 \leq z < 0.45$	$8.60^{0.49}_{0.32}$	$8.86^{0.21}_{0.18}$	$8.17^{0.73}_{0.40}$
$0.45 \leq z < 0.60$	$8.75^{0.16}_{0.14}$	$8.98^{0.17}_{0.15}$	$7.98^{0.29}_{0.23}$
$0.60 \leq z < 0.80$	$9.08^{0.19}_{0.16}$	$9.40^{0.01}_{0.01}$	$8.07^{0.26}_{0.21}$
$0.80 \leq z < 1.00$	$9.15^{0.22}_{0.18}$	$9.56^{0.01}_{0.01}$	$8.16^{0.46}_{0.31}$
$1.00 \leq z < 1.20$	$9.08^{0.30}_{0.23}$	$9.35^{0.02}_{0.02}$	$8.21^{0.28}_{0.22}$
$1.20 \leq z < 1.70$	$9.35^{0.09}_{0.08}$	$9.64^{0.02}_{0.02}$	$8.56^{0.45}_{0.31}$
$1.70 \leq z < 2.00$	$9.63^{0.02}_{0.02}$	$9.89^{0.03}_{0.03}$	$8.83^{0.26}_{0.21}$
$2.00 \leq z < 2.50$	$9.43^{0.13}_{0.12}$	$9.81^{0.03}_{0.03}$	$8.83^{0.36}_{0.26}$
$2.50 \leq z < 3.00$	$9.52^{0.03}_{0.03}$	$9.58^{0.02}_{0.02}$	$8.84^{0.12}_{0.11}$
$3.00 \leq z < 4.20$	$9.75^{0.04}_{0.04}$	$9.14^{0.01}_{0.01}$	$8.73^{0.21}_{0.17}$
$4.20 \leq z < 6.00$	$9.48^{0.08}_{0.08}$	$8.64^{0.02}_{0.02}$	$8.27^{0.07}_{0.07}$

2 onwards. Our highest redshift bin was thought to suffer from incompleteness, but if it is incomplete, the ZFOURGE ρ_{IR} value in this bin does not obviously show it. We see good agreement with the literature out from $0 < z < 2$. Importantly, we do not find a turnover in the IR luminosity density at $z \approx 2$. This is a very different result than is often published in the literature (Gruppioni et al. 2013; Madau & Dickinson 2014; Magnelli et al. 2013; Lutz 2014) (and references within) although this is not a new result as is seen in Rodighiero et al. (2010), but it is likely they do not probe to a sufficiently high enough redshift to capture the decline above $z = 2$.

The CIGALE decomposed SF IR luminosity density is seen to increase from $0 < z < 2$ and subsequently decline from $z > 2$ onwards. This is in agreement with the majority of literature in the IR regime, and indeed from other wavelengths too (cite). The turn over in the star-formation rate density (SFRD) is hotly debated (cite). However, the fact that CIGALE is able to recover the turnover in the SF ρ_{IR} when the ZFOURGE results do not show a turn over in ρ_{IR} at all is impressive and leads us to believe our results are correct. The CIGALE SF luminosity density is elevated above the literature by at most ≈ 1 dex in all redshift bins. We believe this is not an error on CIGALE's part or the ZFOURGE data it is based on, but a representation of the true pure SF IR luminosity density because AGN contaminants have been effectively eliminated. As mentioned previously in section 5.1, both Fu et al. (2010) and Wu et al. (2011) argue that when AGN are removed, the luminosity function is better fit with a Schechter function. This both agrees with our results and explains why our CIGALE luminosity function 4 are elevated over the literature. Thus, integrating under the CIGALE SF Schechter functions, we see an elevation in ρ_{IR} . The evolution of the CIGALE SF luminosity function shown in figure 6 agrees well with CIGALE SF ρ_{IR} . We consistently see that, according to the evolution of the characteristic density ϕ^* , the number of star-forming galaxies has been increasing since the dawn of cosmic time. However, the characteristic luminosity L^* , has been declining since $z \approx 2$. Therefore, our results reaffirm that $z \approx 2$ (approximately 10 Gyrs ago or 3 Gyrs after The Big Bang) is an extremely important epoch for galaxy evolution.

The CIGALE AGN luminosity density follows a similar evolution to literature, but always shows a lower ρ_{IR} . The trend of

ρ_{IR} increasing from $0 < z < 2$ and declining from $z > 2$ onwards appears to still be present. The peak of AGN ρ_{IR} occurs somewhere in the range of $1.85 < z < 2.75$. It seems probable that AGN activity begins to decline ≈ 1 Gyr before SF activity peaks and declines. This hints at a possible delayed AGN feedback scenario in which the activity of the central engine positively influences star formation (cite). Could it be anything else?. This is not the first time a turn over in the AGN ρ_{IR} has been seen. Symeonidis & Page (2021) presents their IR AGN densities up to $z \approx 2.5$. These results are 1-2 orders of magnitude lower than our results. We attribute this to their use of Aird et al. (2015) X-ray sources which are converted to optical luminosity and then to IR luminosity. Their X-ray selected galaxies likely miss the highly obscured and low-luminosity counterpart that this work recovers. As Symeonidis & Page (2021) only extend as far as $z \approx 2.5$, the turn over in the AGN ρ_{IR} is not well constrained. The Delvecchio et al. (2014) AGN agree well with our results. We recomputed the AGN ρ_{IR} of Delvecchio et al. (2014) AGN because they do not list ρ_{IR} and instead focus on the black hole accretion rate density, Ψ_{bhar} . Using the function parameters listed we use the same method described previously to calculate ρ_{IR} . Both Symeonidis & Page (2021) and Delvecchio et al. (2014) show AGN density peaks at $z \approx 2$. This implies an AGN feedback scenario in which central engine activity positively influences star formation at or around the same time cite.

As was mentioned in 5.2, there appeared to be a significant evolutionary epoch for AGN occurring at $z \approx 1$. Similar parameter evolution was seen in Delvecchio et al. (2014), although they only have three redshift bins at or below $z = 1$. Despite the parameter evolution 6 seemingly hinting at a significant cosmic epoch for AGN evolution, we cannot see this reflected in our AGN ρ_{IR} results. From $0 < z < 1$, AGN density is seen to decline, albeit very slowly and with some scatter. Our two lowest redshift bins have very high uncertainties, so there remains the possibility that somewhere between $0 < 1 < z$ is a significant time for AGN evolution.

5.4. Space Density Evolution

We inspect the evolution of different luminosity classes by visualising the number density of luminosities across redshift (figure 8). When possible, the ϕ values are taken from the existing values. Otherwise, ϕ values are calculated from the best fitting luminosity function (figure 4). The class density evolution (figure 8) can be thought of as the transposition of the luminosity function (figure 4). The luminosity function and class density are both complementary in that they allow us to view the number density both as an evolution with luminosity and redshift respectively.

- 1
- 2
- 3

Figure 8 results are significant. We find that the space density of ZFOURGE luminous and ultraluminous IR galaxies (LIRGs, $10^{11} < L_{IR} < 10^{12} L_\odot$ and ULIRGs, $L_{IR} > 10^{12} L_\odot$) have been consistently declining since at least $z = 2$, and very likely even earlier for ULIRGs. Galaxies fainter than LIRGs ($L_{IR} < 10^{11} L_\odot$) begin to decline at a lower redshift than their brighter luminosity counterparts. The redshift at which galaxies begin declining is related to the luminosity of said galaxies. ZFOURGE galaxies fainter than ($L_{IR} < 10^9 L_\odot$) appear to be increasing in number density across

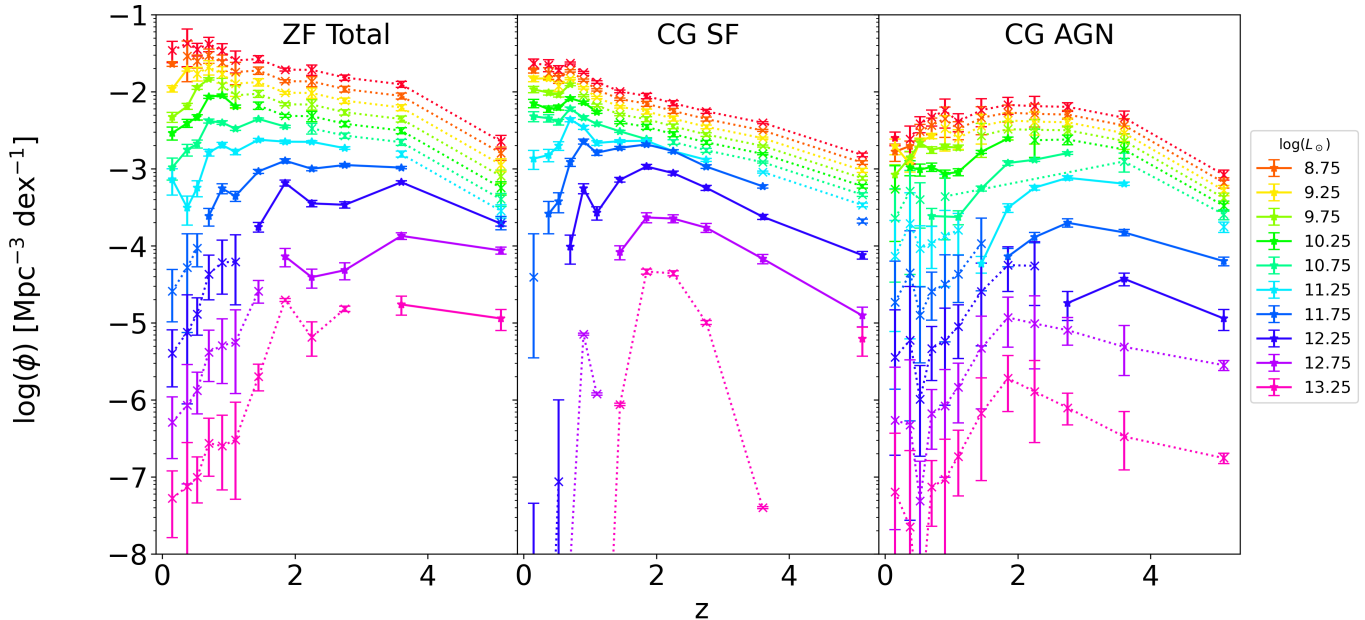


Figure 8: Luminosity class evolution as a function of redshift. ϕ values connected by straight lines correspond to real calculated values. ϕ values connected by dotted lines are estimated from the best fitting function (Schechter for CIGALE SF, Saunders for ZFOURGE Total and CIGALE AGN). Error bars represent the 1σ uncertainty calculated with equation 4 for real values or derived from the function fitting process for estimated values. Real luminosity classes are $0.5 \log(L_\odot)$ in width and centered in the middle (e.g. 8.5 — 9.0 is centred on 8.75). Estimated classes are calculated at the centre of the luminosity bin (e.g. 8.75).

all of cosmic time and have yet to begin declining, if they will at all.

We find similar agreement in the literature with Rodighiero et al. (2010) and Gruppioni et al. (2013) (other references?) results mostly in agreement with ours. ZFOURGE LIRG and ULIRG number densities are elevated.

Our highest redshift bin (centered on $z = 5.1$) is incomplete, and so the ϕ values here should be taken as a lower limit. In that case, it seems highly likely that ULIRGs have been declining in number density since at least $z = 5$ when the universe was barely more than 1 Gyr old, and declining faster since $z = 2$. Luminosity IR galaxies (LIRGs, $10^{11} < L_{IR} < 10^{12} L_\odot$) evolve very differently, showing little evolution in space density between $1 < z < 5$ (accounting for incompleteness in the highest redshift bin). However, LIRGs begin to rapidly decline in space density from $z = 1$ when the universe was 5.7 Gys old to the present day. We find that galaxies with luminosities $L_{IR} < 10^{11} L_\odot$ dominate the IR source density beginning at $z = 0$ all the way up to $z = 2$, where LIRGs very shortly become the dominant class to $z = 3$, after which ULIRGS become the dominate luminosity class onwards. These results indicate that the brightest galaxies have been declining in number very shortly after the Big Bang. More luminous galaxies decline faster and at an earlier time period. Less luminous galaxies take much longer to begin declining.

We present IR luminosity classes as low as $L_{IR} = 10^{8.5} L_\odot$ in figure 8. It is clear that ULIRGs decline much earlier than LIRGs, and LIRGs decline earlier than fainter IR galaxies. This presents a clear trend of brighter objects declining in number density more rapidly than fainter galaxies. Across our data, we only have two luminosity bins between $10^{8.5} < L_{IR} < 10^9$ in the lowest redshift bin only, so results for this luminosity class could be improved in future work. Nevertheless, our results indicate very little number

density evolution across all redshifts measured in our lowest luminosity class $L_{IR} = 10^{8.5} L_\odot$. At $L_{IR} = 10^9 & 10^{9.5} L_\odot$ there is again very little evolution until $z \approx 0.5$ when the number density again begins to decline. These results across a wider range of luminosities and redshifts previously measured in the literature confirm a *downsizing* effect of all luminosity classes, of which the brightest galaxies begin declining before fainter ones.

6. Conclusion

Acknowledgements

Thank you to the anonymous referee that provided feedback on the paper.

Data Availability

Python notebooks and scripts that analysed the data are available on GitHub at <https://github.com/daniel-lyon/MPhil-Code>

References

- Aird, J., Coil, A. L., Georgakakis, A., et al. 2015, Monthly Notices of the Royal Astronomical Society, 451, 1892, doi: [10.1093/mnras/stv1062](https://doi.org/10.1093/mnras/stv1062)
- Assef, R. J., Kochanek, C. S., Ashby, M. L. N., et al. 2011, The Astrophysical Journal, 728, 56, doi: [10.1088/0004-637X/728/1/56](https://doi.org/10.1088/0004-637X/728/1/56)
- Astropy Collaboration, Price-Whelan, A. M., Lim, P. L., et al. 2022, The Astrophysical Journal, 935, 167, doi: [10.3847/1538-4357/ac7c74](https://doi.org/10.3847/1538-4357/ac7c74)
- Biviano, A., Fadda, D., Durret, F., Edwards, L. O. V., & Marleau, F. 2011, Astronomy and Astrophysics, 532, A77, doi: [10.1051/0004-6361/201016174](https://doi.org/10.1051/0004-6361/201016174)
- Boquien, M., Burgarella, D., Roehlly, Y., et al. 2019, Astronomy and Astrophysics, 622, A103, doi: [10.1051/0004-6361/201834156](https://doi.org/10.1051/0004-6361/201834156)
- Brown, A., Nayyeri, H., Cooray, A., et al. 2019, The Astrophysical Journal, 871, 87, doi: [10.3847/1538-4357/aaf73b](https://doi.org/10.3847/1538-4357/aaf73b)

- Caputi, K. I., Lagache, G., Yan, L., et al. 2007, *The Astrophysical Journal*, 660, 97, doi: [10.1086/512667](https://doi.org/10.1086/512667)
- Cowley, M. J., Spitler, L. R., Tran, K.-V. H., et al. 2016, *Monthly Notices of the Royal Astronomical Society*, 457, 629, doi: [10.1093/mnras/stv2992](https://doi.org/10.1093/mnras/stv2992)
- Dai, X., Assef, R. J., Kochanek, C. S., et al. 2009, *The Astrophysical Journal*, 697, 506, doi: [10.1088/0004-637X/697/1/506](https://doi.org/10.1088/0004-637X/697/1/506)
- Delvecchio, I., Gruppioni, C., Pozzi, F., et al. 2014, *Monthly Notices of the Royal Astronomical Society*, 439, 2736, doi: [10.1093/mnras/stu130](https://doi.org/10.1093/mnras/stu130)
- Fu, H., Yan, L., Scoville, N. Z., et al. 2010, *The Astrophysical Journal*, 722, 653, doi: [10.1088/0004-637X/722/1/653](https://doi.org/10.1088/0004-637X/722/1/653)
- Giacconi, R., Zirm, A., Wang, J., et al. 2002, *The Astrophysical Journal Supplement Series*, 139, 369, doi: [10.1086/338927](https://doi.org/10.1086/338927)
- Grazian, A., Fontana, A., Santini, P., et al. 2015, *Astronomy and Astrophysics*, 575, A96, doi: [10.1051/0004-6361/201424750](https://doi.org/10.1051/0004-6361/201424750)
- Gruppioni, C., Pozzi, F., Zamorani, G., & Vignali, C. 2011, *Monthly Notices of the Royal Astronomical Society*, 416, 70, doi: [10.1111/j.1365-2966.2011.19006.x](https://doi.org/10.1111/j.1365-2966.2011.19006.x)
- Gruppioni, C., Pozzi, F., Rodighiero, G., et al. 2013, *Monthly Notices of the Royal Astronomical Society*, 432, 23, doi: [10.1093/mnras/stt308](https://doi.org/10.1093/mnras/stt308)
- Han, Y., Dai, B., Wang, B., Zhang, F., & Han, Z. 2012, *Monthly Notices of the Royal Astronomical Society*, 423, 464, doi: [10.1111/j.1365-2966.2012.20890.x](https://doi.org/10.1111/j.1365-2966.2012.20890.x)
- Harris, C. R., Millman, K. J., van der Walt, S. J., et al. 2020, *Nature*, 585, 357, doi: [10.1038/s41586-020-2649-2](https://doi.org/10.1038/s41586-020-2649-2)
- Hopkins, P. F., Richards, G. T., & Hernquist, L. 2007, *The Astrophysical Journal*, 654, 731, doi: [10.1086/509629](https://doi.org/10.1086/509629)
- Huang, J. S., Ashby, M. L. N., Barmby, P., et al. 2007, *The Astrophysical Journal*, 664, 840, doi: [10.1086/519241](https://doi.org/10.1086/519241)
- Katsianis, A., Blanc, G., Lagos, C. P., et al. 2017, *Monthly Notices of the Royal Astronomical Society*, 472, 919, doi: [10.1093/mnras/stx2020](https://doi.org/10.1093/mnras/stx2020)
- Kennicutt, Jr., R. C. 1998, *The Astrophysical Journal*, 498, 541, doi: [10.1086/305588](https://doi.org/10.1086/305588)
- Lawrence, A., Warren, S. J., Almaini, O., et al. 2007, *Monthly Notices of the Royal Astronomical Society*, 379, 1599, doi: [10.1111/j.1365-2966.2007.12040.x](https://doi.org/10.1111/j.1365-2966.2007.12040.x)
- Leja, J., Johnson, B. D., Conroy, C., van Dokkum, P. G., & Byler, N. 2017, *The Astrophysical Journal*, 837, 170, doi: [10.3847/1538-4357/aa5ffe](https://doi.org/10.3847/1538-4357/aa5ffe)
- Lutz, D. 2014, *Annual Review of Astronomy and Astrophysics*, 52, 373, doi: [10.1146/annurev-astro-081913-035953](https://doi.org/10.1146/annurev-astro-081913-035953)
- Madau, P., & Dickinson, M. 2014, *Annual Review of Astronomy and Astrophysics*, 52, 415, doi: [10.1146/annurev-astro-081811-125615](https://doi.org/10.1146/annurev-astro-081811-125615)
- Magnelli, B., Popesso, P., Berta, S., et al. 2013, *Astronomy and Astrophysics*, 553, A132, doi: [10.1051/0004-6361/201321371](https://doi.org/10.1051/0004-6361/201321371)
- O'Connor, J. A., Rosenberg, J. L., Satyapal, S., & Secrest, N. J. 2016, *Monthly Notices of the Royal Astronomical Society*, 463, 811, doi: [10.1093/mnras/stw1976](https://doi.org/10.1093/mnras/stw1976)
- Persson, S. E., Murphy, D. C., Smee, S., et al. 2013, *Publications of the Astronomical Society of the Pacific*, 125, 654, doi: [10.1086/671164](https://doi.org/10.1086/671164)
- Robotham, A. S. G., Bellstedt, S., Lagos, C. d. P., et al. 2020, *Monthly Notices of the Royal Astronomical Society*, 495, 905, doi: [10.1093/mnras/staa1116](https://doi.org/10.1093/mnras/staa1116)
- Rodighiero, G., Vaccari, M., Franceschini, A., et al. 2010, *Astronomy and Astrophysics*, 515, A8, doi: [10.1051/0004-6361/200912058](https://doi.org/10.1051/0004-6361/200912058)
- Sanders, D. B., Mazzarella, J. M., Kim, D. C., Surace, J. A., & Soifer, B. T. 2003, *The Astronomical Journal*, 126, 1607, doi: [10.1086/376841](https://doi.org/10.1086/376841)
- Saunders, W., Rowan-Robinson, M., Lawrence, A., et al. 1990, *Monthly Notices of the Royal Astronomical Society*, 242, 318, doi: [10.1093/mnras/242.3.318](https://doi.org/10.1093/mnras/242.3.318)
- Schechter, P. 1976, *The Astrophysical Journal*, 203, 297, doi: [10.1086/154079](https://doi.org/10.1086/154079)
- Schmidt, M. 1968, *The Astrophysical Journal*, 151, 393, doi: [10.1086/149446](https://doi.org/10.1086/149446)
- Scoville, N., Aussel, H., Brusa, M., et al. 2007, *The Astrophysical Journal Supplement Series*, 172, 1, doi: [10.1086/516585](https://doi.org/10.1086/516585)
- Spitler, L. R., Labb  , I., Glazebrook, K., et al. 2012, *The Astrophysical Journal*, 748, L21, doi: [10.1088/2041-8205/748/2/L21](https://doi.org/10.1088/2041-8205/748/2/L21)
- Straatman, C. M. S., Spitler, L. R., Quadri, R. F., et al. 2016, *The Astrophysical Journal*, 830, 51, doi: [10.3847/0004-637X/830/1/51](https://doi.org/10.3847/0004-637X/830/1/51)
- Symeonidis, M., & Page, M. J. 2019, *Monthly Notices of the Royal Astronomical Society*, 485, L11, doi: [10.1093/mnrasl/slz022](https://doi.org/10.1093/mnrasl/slz022)
- . 2021, *Monthly Notices of the Royal Astronomical Society*, 503, 3992, doi: [10.1093/mnras/stab598](https://doi.org/10.1093/mnras/stab598)
- Thorne, J. E., Robotham, A. S. G., Davies, L. J. M., et al. 2022, *Monthly Notices of the Royal Astronomical Society*, 509, 4940, doi: [10.1093/mnras/stab3208](https://doi.org/10.1093/mnras/stab3208)
- Virtanen, P., Gommers, R., Oliphant, T. E., et al. 2020, *Nature Methods*, 17, 261, doi: [10.1038/s41592-019-0686-2](https://doi.org/10.1038/s41592-019-0686-2)
- Wu, Y., Shi, Y., Helou, G., et al. 2011, *The Astrophysical Journal*, 734, 40, doi: [10.1088/0004-637X/734/1/40](https://doi.org/10.1088/0004-637X/734/1/40)
- Wuyts, S., Labb  , I., F  rster Schreiber, N. M., et al. 2008, *The Astrophysical Journal*, 682, 985, doi: [10.1086/588749](https://doi.org/10.1086/588749)
- Wylezalek, D., Vernet, J., De Breuck, C., et al. 2014, *The Astrophysical Journal*, 786, 17, doi: [10.1088/0004-637X/786/1/17](https://doi.org/10.1088/0004-637X/786/1/17)